

Phase-space dependence of particle-ratio fluctuations in Pb + Pb collisions from 20A to 158A GeV beam energy

T. Anticic,¹ B. Baatar,² J. Bartke,³ H. Beck,⁴ L. Betev,⁵ H. Białkowska,⁶ C. Blume,⁴ B. Boimska,⁶ J. Book,⁴ M. Botje,⁷ P. Bunčić,⁵ P. Christakoglou,⁷ P. Chung,⁸ O. Chvala,⁹ J. Cramer,¹⁰ V. Eckardt,¹¹ Z. Fodor,¹² P. Foka,¹³ V. Friese,¹³ M. Gaździcki,^{4,14} K. Grebieszko,¹⁵ C. Höhne,¹³ K. Kadija,¹ A. Karev,⁵ V. Kolesnikov,² M. Kowalski,³ D. Kresan,¹³ A. Laszlo,¹² R. Lacey,⁸ M. van Leeuwen,⁷ M. Maćkowiak-Pawłowska,^{4,15} M. Makariev,¹⁶ A. Malakhov,² G. Melkumov,² M. Mitrovski,⁴ S. Mrówczyński,¹⁴ G. Pála,¹² A. Panagiotou,¹⁷ W. Peryt,¹⁵ J. Pluta,¹⁵ D. Prindle,¹⁰ F. Pühlhofer,¹⁸ R. Renfordt,⁴ C. Roland,¹⁹ G. Roland,¹⁹ M. Rybczyński,¹⁴ A. Rybicki,³ A. Sandoval,¹³ A. Rustamov,^{4,*} N. Schmitz,¹¹ T. Schuster,⁴ P. Seyboth,¹¹ F. Siklér,¹² E. Skrzypczak,²⁰ M. Słodkowski,¹⁵ G. Stefanek,¹⁴ R. Stock,⁴ H. Ströbele,⁴ T. Susa,¹ M. Szuba,¹⁵ D. Varga,²¹ M. Vassiliou,¹⁷ G. Veres,¹² G. Vesztergombi,¹² D. Vranić,¹³ Z. Włodarczyk,¹⁴ and A. Wojtaszek-Szwarc¹⁴
(NA49 Collaboration)

¹Rudjer Boskovic Institute, Zagreb, Croatia

²Joint Institute for Nuclear Research, Dubna, Russia

³H. Niewodniczański Institute of Nuclear Physics, Polish Academy of Sciences, Cracow, Poland

⁴Fachbereich Physik der Universität, Frankfurt, Germany

⁵CERN, Geneva, Switzerland

⁶National Center for Nuclear Research, Warsaw, Poland

⁷NIKHEF, Amsterdam, Netherlands

⁸Department of Chemistry, Stony Brook University (SUNYSB), Stony Brook, New York, USA

⁹Institute of Particle and Nuclear Physics, Charles University, Prague, Czech Republic

¹⁰Nuclear Physics Laboratory, University of Washington, Seattle, Washington, USA

¹¹Max-Planck-Institut für Physik, Munich, Germany

¹²Wigner Research Center for Physics, Hungarian Academy of Sciences, Budapest, Hungary

¹³GSI Helmholtzzentrum für Schwerionenforschung GmbH, Darmstadt, Germany

¹⁴Institute of Physics, Jan Kochanowski University, Kielce, Poland

¹⁵Faculty of Physics, Warsaw University of Technology, Warsaw, Poland

¹⁶Institute for Nuclear Research and Nuclear Energy, BAS, Sofia, Bulgaria

¹⁷Department of Physics, University of Athens, Athens, Greece

¹⁸Fachbereich Physik der Universität, Marburg, Germany

¹⁹MIT, Cambridge, Massachusetts, USA

²⁰Institute for Experimental Physics, University of Warsaw, Warsaw, Poland

²¹Eötvös Loránt University, Budapest, Hungary

(Received 21 October 2013; published 6 May 2014)

A novel approach, the identity method, was used for particle identification and the study of fluctuations of particle yield ratios in Pb + Pb collisions at the CERN Super Proton Synchrotron (SPS). This procedure allows one to measure the moments of the multiplicity distributions of protons (p), kaons (K), pions (π), and electrons (e) in case of incomplete particle identification. Using these moments the excitation function of the fluctuation measure $\nu_{\text{dyn}}[A, B]$ was measured, with A and B denoting different particle types. The obtained energy dependence of ν_{dyn} agrees with previously published NA49 results on the related measure σ_{dyn} . However, $\nu_{\text{dyn}}[K, p]$ and $\nu_{\text{dyn}}[K, \pi]$ were found to depend on the phase-space coverage. This feature most likely explains the reported differences between measurements of NA49 and those of STAR in central Au + Au collisions.

DOI: [10.1103/PhysRevC.89.054902](https://doi.org/10.1103/PhysRevC.89.054902)

PACS number(s): 25.75.Gz

I. INTRODUCTION

By colliding heavy ions at high energies one hopes to heat and/or compress the matter to energy densities at which the production of the quark-gluon plasma (QGP) begins [1,2]. Lattice QCD calculations can study this non-perturbative regime of QCD [3] and allow a quantitative investigation of the QGP properties. A first-order phase boundary is expected to separate high-temperature hadron matter from the QGP for

large net baryon density, and is believed to end in a critical point [4]. A wealth of ideas have been proposed to explore the properties and the phase structure of strongly interacting matter. Event-by-event fluctuations of various observables may be sensitive to the transitions between hadronic and partonic phases [5,6]. Moreover, the location of the critical point may be signaled by a characteristic pattern in the energy and system size dependence of the measured fluctuation signals.

Pb + Pb reactions have been investigated at the CERN Super Proton Synchrotron SPS since 1994 by a variety of experiments at the top SPS energy. Many of the predicted signals of the QGP were observed [7], but their uniqueness

*Corresponding author: a.rustamov@cern.ch

was in doubt. Motivated by predictions of the statistical model for the early stage of nucleus-nucleus collisions [8] of characteristic changes of hadron production properties at the onset of QGP creation (onset of the deconfinement), the NA49 experiment performed a scan of the entire SPS energy range, from 158A down to 20A GeV. The predicted features were found at an energy of about 30A GeV in central Pb + Pb collisions [9], thereby indicating the onset of deconfinement in collisions of heavy nuclei in the SPS beam energy range. These observations have recently been confirmed by the Relativistic Heavy Ion Collider (RHIC) beam energy scan, and the expected trend towards higher energy is consistent with Large Hadron Collider (LHC) data [10].

Motivated by these findings, the NA49 Collaboration has started to explore the phase diagram of strongly interacting matter, with the aim of searching for indications of the first-order phase transition and the critical point by studying several measures of fluctuations. In particular, the energy dependence of dynamical event-by-event fluctuations of the particle composition was investigated using the measure $\sigma_{\text{dyn}}(A/B)$ with A and B denoting the multiplicities of different particle species. An increasing trend of σ_{dyn} for both K/p and K/π ratios toward lower collision energies was observed [11–13]. The STAR experiment at the RHIC studies the related event-by-event fluctuation measure ν_{dyn} [14]. In contrast to the measurements of NA49, recent results [15] from the beam energy scan (BES) show practically no energy dependence of $\nu_{\text{dyn}}[K, \pi]$ and a decrease of $\nu_{\text{dyn}}[K, p]$ towards lower energy. The comparison between NA49 and corresponding STAR results was performed using the relation

$$\nu_{\text{dyn}} = \text{sgn}(\sigma_{\text{dyn}})\sigma_{\text{dyn}}^2. \quad (1)$$

However, this relation is only approximate and its accuracy decreases inversely with multiplicity. In order not to rely on this approximation, the fluctuation measure ν_{dyn} was directly reconstructed in this paper using a novel identification scheme, the *identity method* [16,17]. The procedure avoids event-by-event particle ratio fits and the use of mixed events necessary to subtract the artificial correlations introduced by the fits. Moreover, the much improved statistical power allows one to study the effects of the different phase-space coverage of the NA49 (forward rapidities) and STAR (central rapidity, without low- p_{\perp} range) experiments.

The paper is organized as follows. Details about the detector setup and the data are given in Sec. II. Section III discusses the event and track selection criteria. The novel features of this analysis, i.e., the particle identification procedure and the extraction of the moments of the multiplicity distributions, are discussed in Secs. IV and V, respectively. Section VI presents the estimates of statistical and systematic uncertainties. Results on ν_{dyn} and their phase-space dependence are discussed in Secs. VII and VIII. Finally, Sec. IX summarizes the paper.

II. EXPERIMENTAL SETUP AND THE DATA

This paper presents results for central Pb + Pb collisions at projectile energies of 20A, 30A, 40A, 80A, and 158A GeV, recorded by the NA49 experiment (for a detailed description of the NA49 apparatus see Ref. [18]). The principal tracking

detectors are four large-volume time projection chambers (TPCs), with two of them, vertex TPCs (VTPC1 and VTPC2), placed inside superconducting dipole magnets with a combined maximum bending power of 9 T m for a length of 7 m. Care was taken to keep the detector acceptance approximately constant with respect to midrapidity by setting the magnetic field strength proportional to the beam energy. Particle identification in this analysis is achieved by simultaneous measurement of particle momenta and their specific energy loss dE/dx in the gas volume of the main TPCs (MTPC-L and MTPC-R). These are located downstream of the magnets on either side of the beam, have large dimensions (4 m \times 4 m \times 1.2 m), and feature 90 readout pad rows, providing an energy loss measurement with a resolution of about 4%. Two time-of-flight (TOF) scintillator arrays of 891 pixels, each placed behind the MTPCs symmetrically on either side of the beam line, supplement particle identification in a limited region of phase space. In the experiment Pb beams with an intensity of 10^4 ions/s were incident on a thin lead foil located 80 cm upstream of VTPC-1. For 20A–80A GeV and 158A GeV the target thicknesses amounted to 0.224 g/cm² and 0.336 g/cm², respectively. The centrality of a collision was determined based on the energy of projectile spectators measured in the veto calorimeter (VCAL) which is located 26 m behind the target and covers the projectile-spectator phase-space region. A collimator in front of the calorimeter was adjusted for each energy in such a way that all projectile spectator protons, neutrons, and beam fragments could reach the veto calorimeter while keeping the number of produced particles hitting the calorimeter as small as possible.

III. EVENT AND TRACK SELECTION CRITERIA

The only event selection criterion used in this analysis is a centrality cut based on the energy (E_{Cal}) of forward-going projectile spectators measured in VCAL. The data were recorded with an online VCAL cut accepting the 7% and 10% most central Pb + Pb collisions for 20A–80A GeV and 158A GeV, respectively. Using an offline cut on E_{Cal} , event samples of the 3.5% most central reactions were selected, which in the Glauber Monte Carlo model corresponds to about 367 wounded nucleons and an impact parameter range of $0 < b < 2.8$ fm [19]. To ensure better particle separation, only the tracks with large track length (better energy loss resolution) in the MTPCs were used for further analysis. For this purpose we distinguish between the number of potential and the number of reconstructed dE/dx points. The former was estimated according to the position of the track in space together with the known TPC geometry, while the latter represents the number of track points reconstructed by the cluster finder algorithm. In addition, to avoid the usage of track fragments (split tracks from different TPCs which were not matched together), it is required that more than 50% of potential points have to be found by the reconstruction algorithm. The following track selection criteria, referred to as the “loose cuts,” are used for the main analysis:

- (i) The number of reconstructed points in the MTPCs should be more than 30.

TABLE I. The statistics corresponding to the 3.5% most central Pb + Pb collisions, with applied “loose cuts” (“tight cuts”), used in this analysis. The $\langle N^{\text{all}} \rangle$ and $\langle N^{\text{pos.}} \rangle$ stand for the mean number of all and positively charged particles, respectively. Note that N^{events} , the total numbers of analyzed events, are the same for both loose and tight cuts.

Beam energy (GeV)	$\sqrt{s_{N+N}}$ (GeV)	N^{events}	$\langle N^{\text{all}} \rangle$	$\langle N^{\text{pos.}} \rangle$
20A	6.3	169k	63 (56)	46 (41)
30A	7.6	179k	113 (98)	75 (65)
40A	8.7	195k	159 (137)	99 (86)
80A	12.3	136k	315 (262)	181 (153)
158A	17.3	125k	560 (448)	310 (255)

- (ii) The ratio of the number of reconstructed points in all TPCs (VTPCs + MTPCs) to the number of potential points in all TPCs should exceed 0.5.

These selections reduce the acceptance of the particles to the forward rapidity regions in the center-of-mass reference frame. In order to study the systematic uncertainties of the final results due to the applied track cuts another set of cuts (“tight cuts”) was employed in addition to the loose cuts:

- (i) The number of potential points in at least one of the vertex TPCs (VTPC1 or VTPC2) and in the MTPCs should be more than 10 and 30, respectively.
(ii) The ratio of the number of reconstructed points to the number of potential points in the selected TPC(s) should exceed 0.5.
(iii) The distance between the closest point on the extrapolated track to the main vertex position should be less than 4 cm in x (bending plane) and less than 2 cm in y (vertical).

The statistics used in this analysis, with applied loose cuts (tight cuts), is shown in Table I.

IV. PARTICLE IDENTIFICATION

Particle identification (PID) in this analysis is achieved by correlating the measured particle momentum with its specific energy loss in the gas volume of the MTPCs. The key problem of this identification procedure is the large fluctuation of the specific energy loss which has a long tail for large values. The shape of the probability distribution was first calculated in Ref. [20] and is referred to as the Landau distribution. To improve the resolution of the specific energy loss measurement, multiple sample measurements in pad rows along the track are performed. Then the specific energy loss dE/dx of the track is calculated as a truncated mean [18] of the distribution of the sample measurements. To obtain the contributions of different particle species, fits of the inclusive distributions (obtained for tracks from all events) of dE/dx (see Refs. [21,22] for details) were performed separately for negatively and positively charged particles in bins of total laboratory momentum (p), transverse momentum (p_{\perp}), and azimuthal angle (ϕ). Bins with less than 3000 entries were

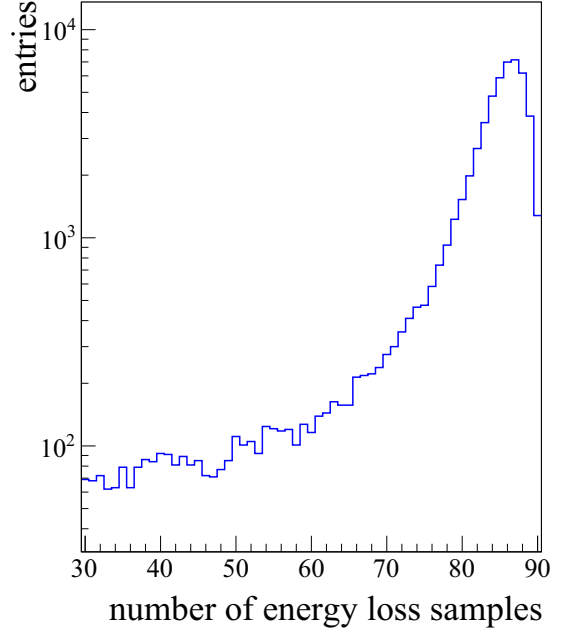


FIG. 1. (Color Online) Distribution of number of measured energy loss samples per track for the phase-space bin $5.2 < p < 6.4$ GeV/c, $0.4 < p_{\perp} < 0.6$ GeV/c, and $135^{\circ} < \phi < 180^{\circ}$ at 20A GeV.

not used in the analysis to ensure sufficient statistics in each bin for the fitting algorithm. The distribution of the number of measured energy loss samples per track in a representative bin is illustrated in Fig. 1. The distribution of measured dE/dx values for each particle type j ($j = p, K, \pi, e$) is represented by a weighted sum of Gaussian functions:

$$F_j\left(\frac{dE}{dx} \equiv x\right) = \frac{1}{C} \sum_n \frac{N_n}{\sqrt{2\pi}\sigma_{j,n}} \exp\left[-\frac{1}{2} \left(\frac{x - \bar{x}_j}{(1 \pm \delta)\sigma_{j,n}}\right)^2\right]. \quad (2)$$

Here, N_n is the number of tracks with n measured energy loss samples, \bar{x}_j is the fitted specific energy loss (later referred to as position) of particle type j , and $\sigma_{j,n}$ is the width of the Gaussian distribution which depends on particle type j and the number of samples, n . The asymmetry parameter δ was introduced to account for the tails of the Landau distributions, which are still present even after truncation. In the truncation procedure only the 50% samples with the smallest energy loss values are used to determine the specific energy loss dE/dx [18]. The normalization constant C in Eq. (2) is $\sum_n N_n$, thus normalizing F_j to unity. The width $\sigma_{j,n}$ is parametrized as

$$\sigma_{j,n} = \sigma_0 \left(\frac{\bar{x}_j}{\bar{x}_\pi}\right)^\alpha \frac{1}{\sqrt{N_n}}, \quad (3)$$

where α was estimated from the data and set to 0.625 [21].

The parametrization of the inclusive dE/dx distribution $\rho(x)$ is obtained by summing the functions F_j over the particle types:

$$\rho(x) = \sum_{j=p,K,\pi,e} \rho_j(x) = \sum_{j=p,K,\pi,e} A_j F_j(x) \quad (4)$$

with A_j being the mean multiplicity of particle j in a given bin. As a result of fitting this function to the experimental dE/dx distributions, one obtains in each phase-space bin the yield of particle j , A_j , the ratio of specific energy loss \bar{x}_j/\bar{x}_π , the parameter σ_0 , and the asymmetry parameter δ . The total number of fitted parameters is $2(k + 1)$ with k denoting the number of particles. Obtained fit parameters, which are later used to access the dE/dx distribution functions (DFs) of different particles, are stored in a lookup table. In the case of positive particles, DFs of kaons are masked by the protons and the mean values for protons and kaons cannot be fitted uniquely. To circumvent this problem the fitting procedure was performed in two steps:

- (i) The fitting procedure is started with negatively charged particles. As for the studied energy range the number of antiprotons is small, the pion and kaon peaks are essentially separated. In order to cover a large phase-space region and obtain sufficient statistics, integration is performed over the transverse momentum bins at this stage.
- (ii) The fitting procedure is repeated separately for negatively and positively charged particles in bins of p , p_\perp , and ϕ with the ratio \bar{x}_K/\bar{x}_π fixed from step 1.

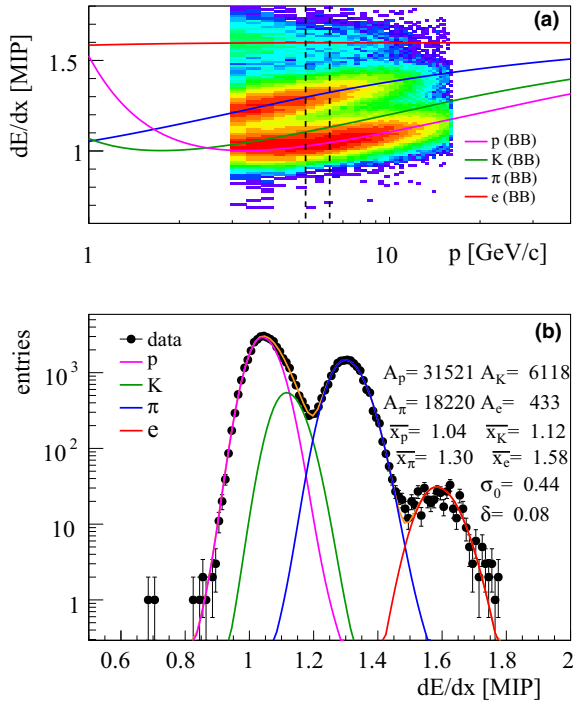


FIG. 2. (Color Online) (a) Measured dE/dx values as function of reconstructed momenta at 20A GeV for the phase-space region $0.4 < p_\perp < 0.6$ GeV/c and $135^\circ < \phi < 180^\circ$. Lines correspond to calculations with the Bethe-Bloch (BB) formula for different particle types. (b) Projection of the upper plot to the vertical axis in the momentum interval $5.2 < p < 6.4$ GeV/c indicated by vertical dashed lines. Colored lines represent the dE/dx distribution functions of different particles using Eq. (2) and the fit parameters listed in the figure.

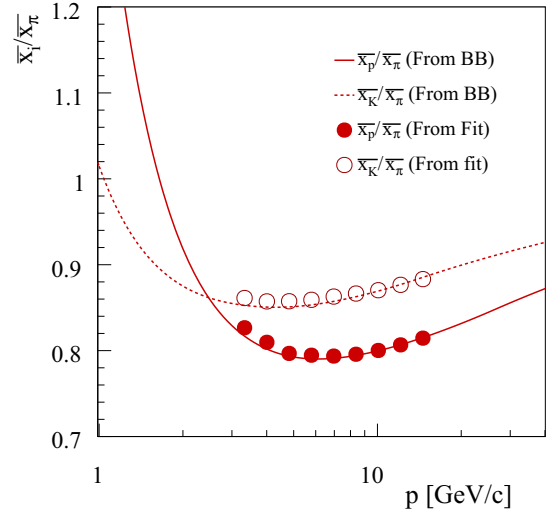


FIG. 3. (Color Online) Ratio of fitted specific energy loss (symbols) compared to corresponding ratios from the Bethe-Bloch parametrization (curves) for 20A GeV data. The deviations of the fitted values from the Bethe-Bloch curves are below 1 %.

As an example, we present in the upper panel of Fig. 2 a plot of measured dE/dx values versus the reconstructed momenta. The lower panel of Fig. 2 shows the projection of the upper plot onto the dE/dx axis in the selected momentum interval indicated by dashed vertical lines. The distribution functions of different particles obtained from Eq. (2) using the fit parameters listed in the figure are displayed by colored lines.

In Fig. 3 the ratios of specific energy loss of different particles are compared to the corresponding ratios from the Bethe-Bloch parametrization. Figure 4 demonstrates the separation between fitted specific energy loss values of kaons and protons quantified as $|\bar{x}_p - \bar{x}_K|/\sigma$ with x_p and x_K

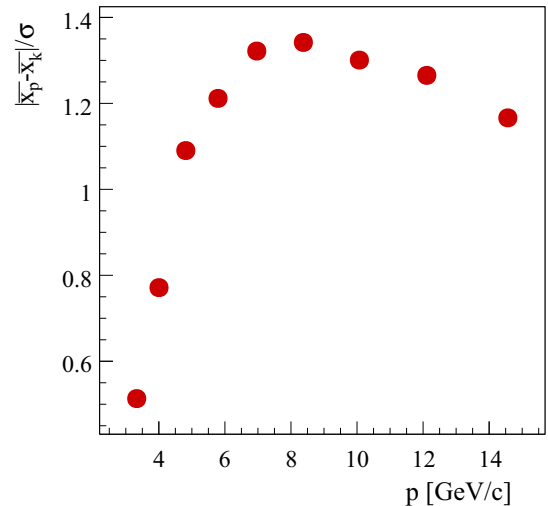


FIG. 4. (Color Online) The difference between specific energy loss of kaons and protons normalized to the dE/dx width for 20A GeV data.

denoting the specific energy loss values for protons and kaons respectively, and σ stands for $\sqrt{\sigma_p^2 + \sigma_K^2}$. Here the σ_j ($j = p, K$) is calculated as

$$\sigma_j = \frac{1}{C} \sum_n \sigma_{j,n}, \quad (5)$$

with C and $\sigma_{j,n}$ defined in Eqs. (2) and (3), respectively.

V. ANALYSIS METHOD

Most measures proposed for event-by-event fluctuations are defined as functions of moments of the multiplicity distributions. In particular, the fluctuation measure ν_{dyn} depends on the first and all second (pure and mixed) moments of the multiplicity distributions of the studied particles species. For example, the second (pure) moment for pions and the second mixed moment for protons and pions are defined as

$$\langle N_\pi^2 \rangle = \sum_{N_\pi=0}^{\infty} N_\pi^2 P(N_\pi), \quad (6)$$

and

$$\langle N_\pi N_p \rangle = \sum_{N_\pi=0}^{\infty} \sum_{N_p=0}^{\infty} N_\pi N_p P(N_p, N_\pi), \quad (7)$$

where $P(N_\pi)$ is the probability distribution of pion multiplicity, while $P(N_p, N_\pi)$ is the joint probability distribution for pion and proton multiplicities. N_π and N_p in Eqs. (6) and (7) stand for the pion and proton multiplicities.

The standard approach of finding the moments is to count the number of particles event by event. However, this approach is hampered by incomplete particle identification (overlapping dE/dx distribution functions), which can be taken care of by either selecting suitable phase-space regions (where the distribution functions do not overlap) or by applying an event-by-event fitting procedure. The latter typically introduces artificial correlations which are usually corrected for by the event mixing technique. Here a novel approach, called the *identity method* [16,17,23], is applied for the first time. The method follows a probabilistic approach which avoids the event-by-event fitting and determines the moments of the multiplicity distributions by an unfolding procedure which has a rigorous mathematical derivation [17]. Thus there is no need for corrections based on event mixing. The method employs the fitted inclusive dE/dx distribution functions of particles, $\rho_j(x)$, with j standing for proton, kaon, pion, and electron. Each event has a set of measured dE/dx values, x_i , corresponding to each track in the event. For each track in an event a probability w_j was estimated of the track being from particle j ,

$$w_j(x_i) \equiv \frac{\rho_j(x_i)}{\rho(x_i)}, \quad (8)$$

where the values of ρ and ρ_j are calculated using the parameters stored in the lookup table of fitted DFs in the appropriate phase-space bin, and

$$\rho(x_i) \equiv \sum_{j=p,K,\pi,e} \rho_j(x_i). \quad (9)$$

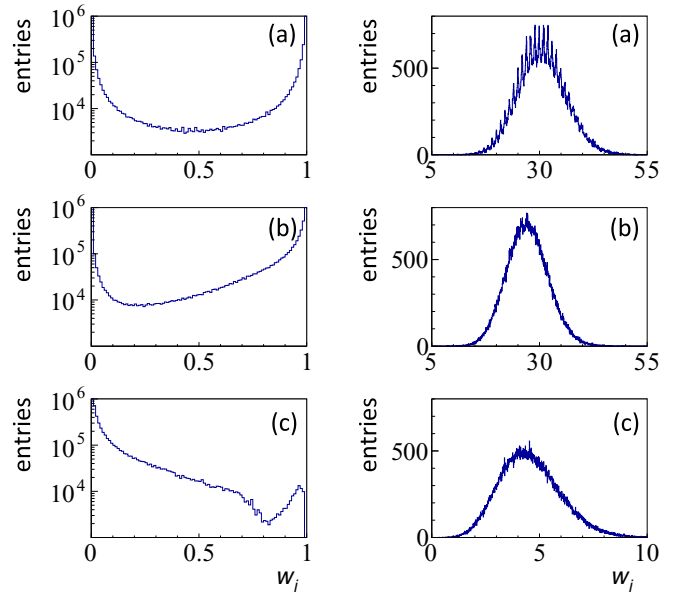


FIG. 5. (Color Online) Left panel: Distributions of w_j of Eq. (8) for (a) pions, (b) protons, and (c) kaons for 20A GeV data. Right panel: Corresponding distributions of W_j of Eq. (10).

Note that the ρ_j functions are just DFs normalized to the mean multiplicity of particle j . Further, an event variable (an approximation of the multiplicity of particle j in the event) W_j is defined as

$$W_j = \sum_{i=1}^n w_j(x_i), \quad (10)$$

where n is the total number of selected tracks in the given event. Examples of distributions of w_j and W_j for π , K , and p are shown in Fig. 5.

TABLE II. Upper part: Mean multiplicities of $p + \bar{p}$, $\pi^+ + \pi^-$, and $K^+ + K^-$ for the 3.5% most central Pb + Pb collisions calculated by summing the integrals of respective DFs over phase-space bins. Lower part: Reconstructed second moments of the multiplicity distributions of $p + \bar{p}$, $\pi^+ + \pi^-$, and $K^+ + K^-$ for the 3.5% most central Pb + Pb collisions. The mixed moments are presented in terms of covariances, $\text{Cov}[N_1, N_2] = \langle N_1 N_2 \rangle - \langle N_1 \rangle \langle N_2 \rangle$. For 20A and 30A GeV, values for $\text{Cov}[N_p, N_K]$ and $\text{Cov}[N_p, N_\pi]$ are negative. Numerical values with higher precision are available in Ref. [24]. These are required to reproduce the values of ν_{dyn} shown in this paper.

	20A GeV	30A GeV	40A GeV	80A GeV	160A GeV
$\langle N_p \rangle$	27.1	34.7	38.0	47.0	68.7
$\langle N_\pi \rangle$	30.5	66.4	103.0	226.7	414.6
$\langle N_K \rangle$	4.7	9.4	13.9	31.5	57.8
$\langle N_p^2 \rangle$	759.94	1238.09	1475.89	2254.35	4780.52
$\langle N_\pi^2 \rangle$	963.6	4485.36	10731.4	51764.4	172811.0
$\langle N_K^2 \rangle$	26.4	98.06	207.27	1030.06	3415.69
$\text{Cov}[N_p, N_\pi]$	2.13	4.34	9.05	22.62	44.03
$\text{Cov}[N_p, N_K]$	-0.75	-0.69	0.39	2.41	10.92
$\text{Cov}[N_K, N_\pi]$	-1.02	-1.39	0.29	15.84	81.75

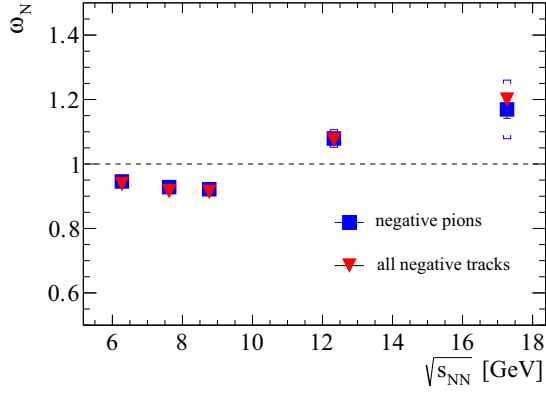


FIG. 6. (Color Online) The energy dependence of the scaled variance ω of the negatively charged pion multiplicity distribution, reconstructed using the identity method, is plotted as blue squares. The red triangles are estimates based on direct event-by-event counting of all negative particles. The remarkable agreement between these results is an experimental verification of the identity method.

As the introduced W_j quantities are calculated for each event, one obtains all second moments of the W_j quantities by straightforward averaging over the events. Finally, using the identity method one unfolds the second moments of the true multiplicity distributions from the moments of the W_j quantities [17]. Obtained results (second moments) for the 3.5% most central Pb + Pb collisions at different projectile energies are listed in the lower part of Table II. The mean

multiplicities (first moments) shown in the upper part of Table II are the results of integration of the respective DFs. The identity method has been successfully tested for numerous simulations in Ref. [23]. A direct experimental verification of the method can be provided by investigating the energy dependence of the scaled variance ω of the negatively charged pion multiplicity distribution, where ω is

$$\omega = \frac{\text{Var}(N)}{\langle N \rangle} = \frac{\langle N^2 \rangle - \langle N \rangle^2}{\langle N \rangle}. \quad (11)$$

For this purpose two independent analyses were performed: (i) using the reconstructed moments for negatively charged pions (from the identity method) and (ii) counting the negatively charged particles event by event (i.e., without employing the identity method). The results of these analyses are presented in Fig. 6 by blue squares for case (i) and by red triangles for case (ii). As the majority of negative particles are pions, the remarkable agreement between the results of these two independent approaches is a direct experimental verification of the identity method.

VI. STATISTICAL AND SYSTEMATIC ERROR ESTIMATES

The statistical errors of the reconstructed moments of the multiplicity distributions result from the errors on the parameters of the fitted distributions $\rho_j(x)$ and from the errors of the W_j quantities. Typically these two sources of errors are correlated. Fluctuation observables are usually built up from several moments of the multiplicity distributions. Since

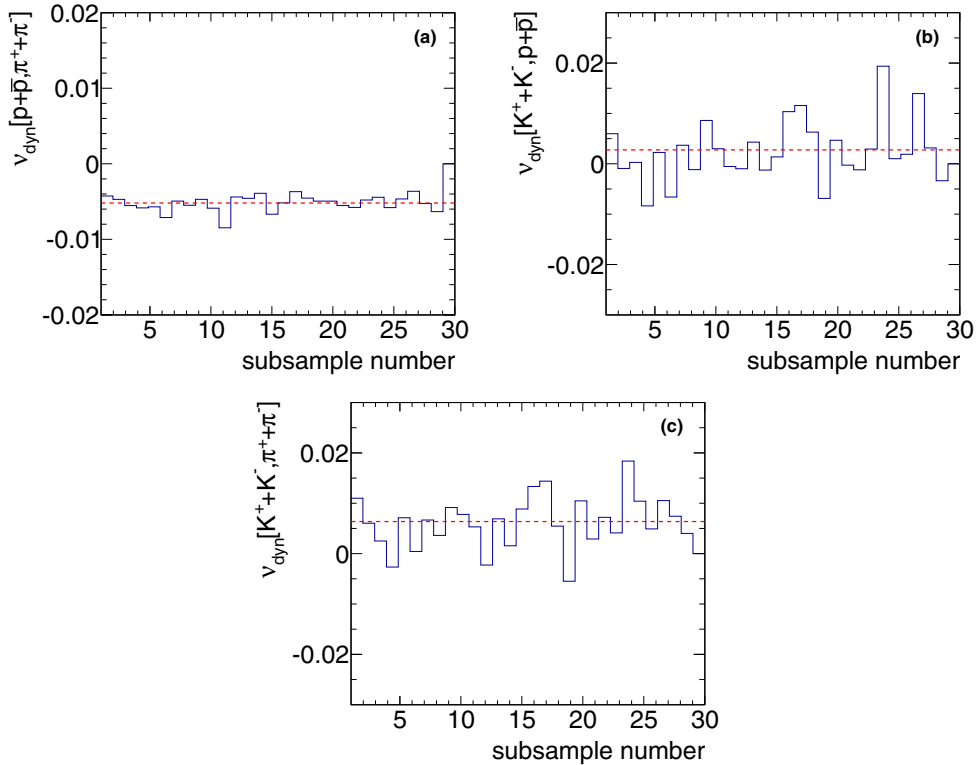


FIG. 7. (Color Online) Reconstructed values of (a) $v_{\text{dyn}}[p + \bar{p}, \pi^+ + \pi^-]$, (b) $v_{\text{dyn}}[K^+ + K^-, p + \bar{p}]$, and (c) $v_{\text{dyn}}[K^+ + K^-, \pi^+ + \pi^-]$ for Pb + Pb collisions at 30A GeV as a function of subsample number. Dashed red lines indicate corresponding averaged values of v_{dyn} over subsamples.

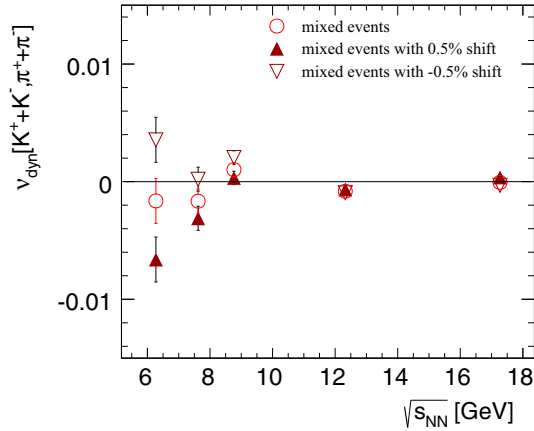


FIG. 8. (Color Online) $v_{\text{dyn}}[K^+ + K^-, \pi^+ + \pi^-]$ for mixed events is shown versus energy by red open circles. Solid (open) red triangles represent the results obtained with the kaon positions shifted artificially by 0.5% (−0.5%).

the standard error propagation is impractical, the subsample approach was chosen to evaluate the statistical uncertainties. One first randomly subdivides the data into n subsamples, and for each subsample then reconstructs the moments M_n listed in

Table II. In the second step the statistical error of each moment M is calculated as

$$\sigma_{(M)} = \frac{\sigma}{\sqrt{n}}, \quad (12)$$

where

$$\langle M \rangle = \frac{1}{n} \sum M_n, \quad (13)$$

and

$$\sigma = \sqrt{\frac{\sum (M_i - \langle M \rangle)^2}{n - 1}}. \quad (14)$$

The same procedure is followed for the fluctuation quantities, e.g., v_{dyn} , which are functions of the moments. An example is shown in Fig. 7.

Next, systematic uncertainties of the analysis procedure are discussed. One possible source of systematic bias might be the specific choice of event and track cuts. In order to obtain an estimate of this uncertainty, results for the moments were derived for loose and tight cuts (see Sec. III). The small observed differences were taken as one component of the systematic error.

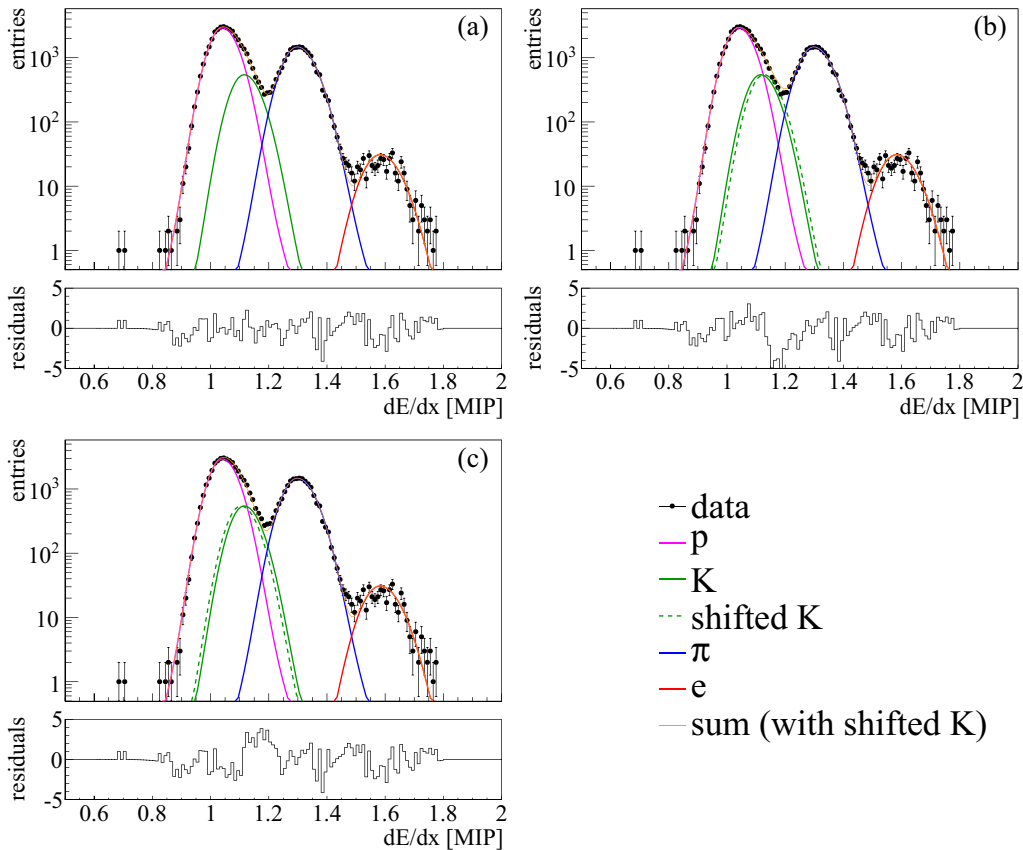


FIG. 9. (Color Online) Energy loss distributions in the selected phase-space bin corresponding to Fig. 2 with superimposed fit functions for protons, pions, kaons, and electrons shown by colored solid lines. The dashed green lines correspond to artificially shifted positions of kaons by 0.5% (b) and −0.5% (c). The shifted distribution functions were used to investigate the systematic errors stemming from the particle identification (dE/dx fitting) procedure. The corresponding residual plots are also presented. The residuals are defined as the difference between data points and the total fit function (indicated by sum), normalized to the statistical error of data points.

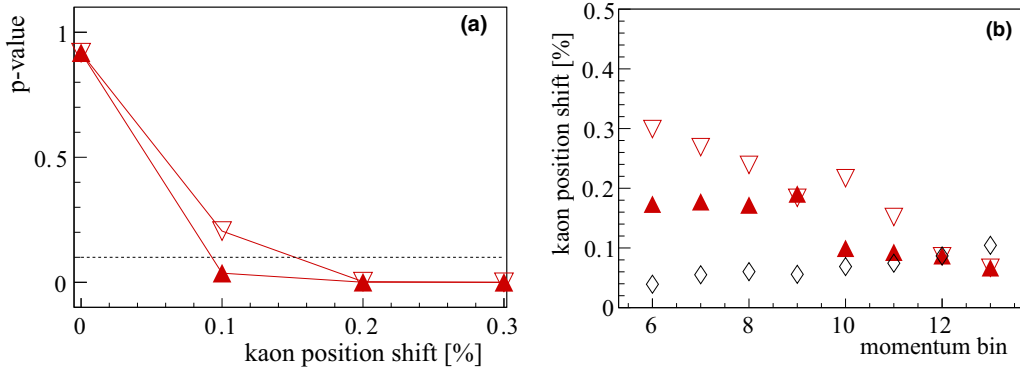


FIG. 10. (Color Online) (a) The p value of the K-S statistics as function of the artificially introduced shifts in the fitted kaon positions for 30A GeV data. The direction of triangles indicates the direction of introduced shifts. The null hypothesis is rejected when the p value is below the significance level of 10, indicated by the dashed line. The maximum value of the kaon shift is taken as the abscissa of the intersection point of full red and dashed black lines. (b) Maximum values of the kaon position shift as function of the momentum in a selected bin of transverse momentum and azimuthal angle. Diamonds represent the statistical errors on kaon positions obtained from the fitting procedure. Note that the left plot is shown for the momentum bin 11, which corresponds to the momentum range of $7.6 < p < 9.1$ GeV/ c .

Possible biases of the identification procedure were studied using mixed events. Each event i was constructed by randomly selecting a reconstructed track (including the dE/dx

measurement) from each of the following j events, with j corresponding to the number of reconstructed tracks in the event i . The results for $v_{\text{dyn}}[K^+ + K^-, \pi^+ + \pi^-]$ for mixed

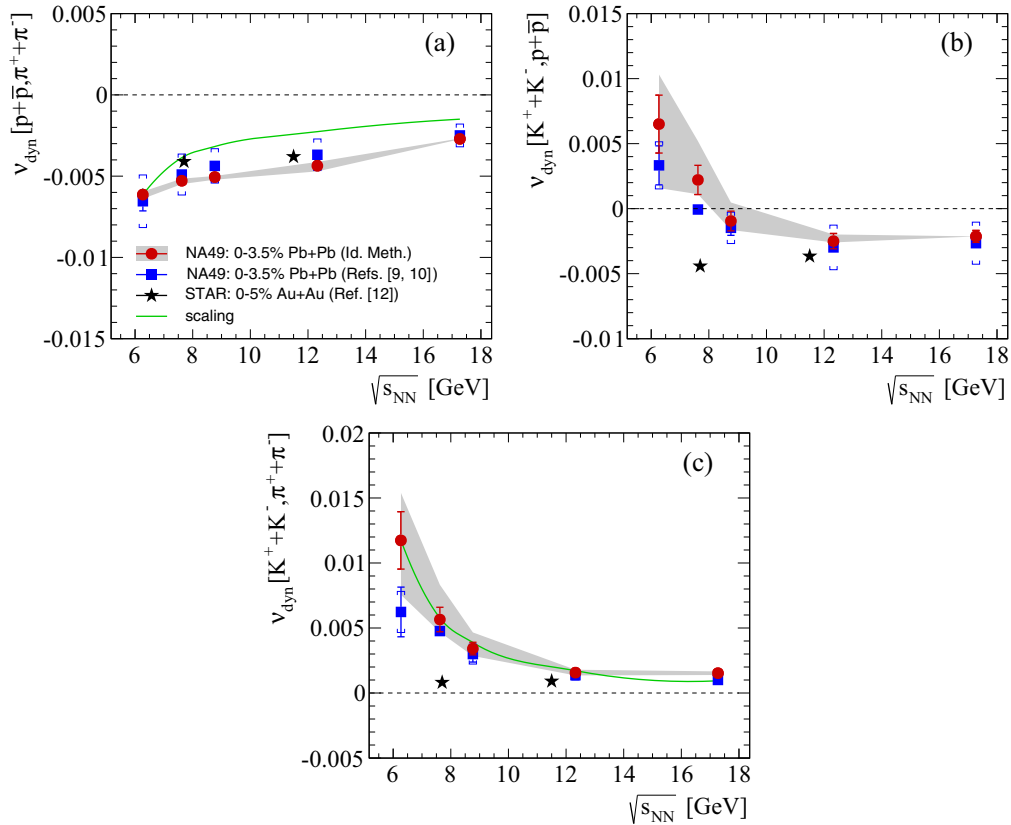


FIG. 11. (Color Online) Energy dependence of (a) $v_{\text{dyn}}[p^+ \bar{p}, \pi^+ + \pi^-]$, (b) $v_{\text{dyn}}[K^+ + K^-, p^+ \bar{p}]$, and (c) $v_{\text{dyn}}[K^+ + K^-, \pi^+ + \pi^-]$. Results from the identity method for central Pb + Pb data of NA49 are shown by red solid circles. Published NA49 results, converted from σ_{dyn} to v_{dyn} using Eq. (1), are indicated by blue squares. Stars represent results of the STAR Collaboration for central Au + Au collisions. In addition, for cases (a) and (c), the energy dependence predicted by Eq. (18) is displayed by the green curves, which are consistent with the experimentally established trend. The systematic errors (see Secs. VI and VII) are presented as shaded bands.

events are presented in Fig. 8 by red open circles. As expected the reconstructed values of ν_{dyn} are vanishing independently of energy.

Furthermore, systematic uncertainties stemming from the quality of the fit functions were investigated with the help of mixed events. Even though the two-step fitting procedure discussed in Sec. IV was used to determine the DFs, it remains a challenge to properly fit the kaon positions. In nearly all relevant phase-space intervals the measured energy loss distributions of kaons are overlapping with those of pions and protons. To study the influence of possible systematic shifts in fit parameters on the extracted moments, the fitted positions of kaons were shifted artificially by 0.5 % in both directions. The dashed green lines in Fig. 9 show the artificially shifted dE/dx distribution functions of kaons. Results for $\nu_{\text{dyn}}[K^+ + K^-, \pi^+ + \pi^-]$ obtained with these shifted kaon distribution functions for the mixed events are plotted as red triangles in Fig. 8. At lower beam energies one observes a significant dependence of the results on kaon positions. In order to gain quantitative estimates of a possible shift of the kaon position, we performed hypothesis testing using the Kolmogorov-Smirnov (K-S) statistics. For this purpose we test the null hypothesis that measured dE/dx distributions and fit functions are similar within a given significance level of 10%. We repeat the test by shifting the fitted kaon positions in both directions. The obtained results from the K-S test in a selected phase-space bin are presented in the left panel of Fig. 10 for the 30A GeV data. The maximum value of the kaon position shift is taken to be the abscissa of the intersection point of the red lines with the dashed line. We conclude that with a 10% significance level the null hypothesis is rejected for 0.09% and 0.15% up and down shifts, respectively. In the right panel of Fig. 10 the dependence of the kaon position shift is presented as function of the momentum bin in a selected bin of transverse momentum and azimuthal angle. The shift values for all other phase-space bins were obtained in a similar way.

Emerging systematic errors on the fluctuation measure ν_{dyn} , added in quadrature with other sources of systematics, are depicted in Fig. 11 by the shaded bands (see the next section).

VII. RESULTS ON THE FLUCTUATION MEASURE ν_{dyn}

The measure $\nu_{\text{dyn}}[A, B]$ of dynamical event-by-event fluctuations of the particle composition is defined as [14]

$$\nu_{\text{dyn}}[A, B] = \frac{\langle A(A-1) \rangle}{\langle A \rangle^2} + \frac{\langle B(B-1) \rangle}{\langle B \rangle^2} - 2 \frac{\langle AB \rangle}{\langle A \rangle \langle B \rangle}, \quad (15)$$

where A and B stand for multiplicities of different particle species. As seen from the definition, Eq. (15), the value of ν_{dyn} vanishes when the multiplicity distributions of particles A and B follow the Poisson distribution and when there are no correlations between these particles ($\langle AB \rangle = \langle A \rangle \langle B \rangle$). On the other hand, a positive correlation term reduces the value of ν_{dyn} , while an anticorrelation increases it. Inserting the values of the reconstructed moments (see Ref. [24] for precise values) into Eq. (15) one obtains the values of $\nu_{\text{dyn}}[p + \bar{p}, \pi^+ + \pi^-]$, $\nu_{\text{dyn}}[K^+ + K^-, p + \bar{p}]$, and $\nu_{\text{dyn}}[K^+ + K^-, \pi^+ + \pi^-]$. These results are represented by red solid circles in Fig. 11. Statistical

TABLE III. Numerical values of $0.5 |\nu_{\text{dyn}}^{\text{loose}} - \nu_{\text{dyn}}^{\text{tight}}|$ for different particle pairs.

	$[p + \bar{p}, \pi^+ + \pi^-]$ (10^{-3})	$[K^+ + K^-, p + \bar{p}]$ (10^{-3})	$[K^+ + K^-, \pi^+ + \pi^-]$ (10^{-3})
20A GeV	0.150	0.729	0.363
30A GeV	0.108	0.557	0.633
40A GeV	0.067	0.090	0.180
80A GeV	0.182	0.059	0.034
160A GeV	0.025	0.001	0.139

errors σ_{stat} were estimated using the subsample method discussed in Sec. VI. Systematic uncertainties due to the applied track selection criteria were estimated by calculating ν_{dyn} separately for tracks selected by loose ($\nu_{\text{dyn}}^{\text{loose}}$) and tight ($\nu_{\text{dyn}}^{\text{tight}}$) cuts. The numerical values of $0.5 |\nu_{\text{dyn}}^{\text{loose}} - \nu_{\text{dyn}}^{\text{tight}}|$ are presented in Table III

The systematic errors stemming from the uncertainty of the kaon fit were estimated using the K-S test (see Sec. III). The shift values of the fitted kaon positions, obtained from the K-S test for each phase-space bin, were used to obtain the values of $\nu_{\text{dyn}}^{\text{up}}$ and $\nu_{\text{dyn}}^{\text{down}}$. Final results (red solid circles in Fig. 11) are then presented as

$$\nu_{\text{dyn}}[A, B] = \frac{\nu_{\text{dyn}}^{\text{loose}} + \nu_{\text{dyn}}^{\text{tight}}}{2}, \quad (16)$$

the statistical errors are estimated using Eq. (12), while the systematic errors, presented with shaded areas in Fig. 11 are calculated as

$$\sigma_{\text{sys}}^k = \text{sgn}(\nu_{\text{dyn}}^k - \nu_{\text{dyn}}) \times \sqrt{(\nu_{\text{dyn}}^k - \nu_{\text{dyn}})^2 + \left(\frac{\nu_{\text{dyn}}^{\text{loose}} - \nu_{\text{dyn}}^{\text{tight}}}{2}\right)^2}, \quad (17)$$

with $k = (\text{up}, \text{down})$.

These results (see Fig. 11 and Tables IV, V, and VI) are consistent with the values of ν_{dyn} obtained via Eq. (1) from the previously published NA49 measurements of the related measure σ_{dyn} [11,12] (blue squares in Fig. 11). Note that the source of systematic errors due to the uncertainties in kaon position were not considered in previously published NA49 results, hence the presented systematic errors (blue vertical bars) were underestimated. We thus conclude that the increasing

TABLE IV. Numerical values of $\nu_{\text{dyn}}[p + \bar{p}, \pi^+ + \pi^-]$ with statistical and systematic error estimates.

	ν_{dyn} (10^{-3})	σ_{stat} (10^{-3})	σ_{sys} (10^{-3})
20A GeV	-6.139	± 0.243	+0.251 -0.190
30A GeV	-5.282	± 0.191	+0.206 -0.126
40A GeV	-5.058	± 0.125	+0.160 -0.068
80A GeV	-4.361	± 0.134	+0.346 -0.235
160A GeV	-2.706	± 0.329	± 0.025

TABLE V. Numerical values of $\nu_{\text{dyn}}[K^+ + K^-, p + \bar{p}]$ with statistical and systematic error estimates.

	$\nu_{\text{dyn}} (10^{-3})$	$\sigma_{\text{stat.}} (10^{-3})$	$\sigma_{\text{sys.}} (10^{-3})$
20A GeV	6.503	± 2.226	+3.808 -4.92
30A GeV	2.210	± 1.122	+2.985 -1.099
40A GeV	-0.949	± 0.759	+1.422 -0.693
80A GeV	-2.498	± 0.587	+0.513 -0.099
160A GeV	-2.135	± 0.460	± 0.001

trend of the excitation functions of $\nu_{\text{dyn}}[K^+ + K^-, p + \bar{p}]$ and $\nu_{\text{dyn}}[K^+ + K^-, \pi^+ + \pi^-]$ toward low energies is confirmed by two independent analyses of the NA49 data on central Pb + Pb collisions. Also presented in Fig. 11 are the STAR results (black stars) from the RHIC beam energy scan (BES) program [15] for central Au + Au collisions, which clearly differ at low energies. However, as mentioned above, the phase-space coverage of NA49 and STAR are not the same. The consequences will be discussed below.

VIII. PHASE-SPACE DEPENDENCE OF ν_{dyn} MEASUREMENTS

The investigation presented in this section attempts to shed light on the cause of the differences between the results from STAR and NA49 on fluctuations of identified hadrons. Two sources were studied: the dependence of ν_{dyn} on the multiplicity of the particles entering the analysis and a possible sensitivity of ν_{dyn} to the covered phase-space region.

Indeed, it was argued in Ref. [25] that ν_{dyn} may exhibit a dependence on the multiplicities of accepted particles. Since multiplicities increase with increasing collision energy, the following energy dependence of ν_{dyn} was suggested:

$$\nu_{\text{dyn}}[A, B](E) = \nu_{\text{dyn}}[A, B](E_{\text{ref}}) \frac{\left[\frac{1}{\langle A \rangle} + \frac{1}{\langle B \rangle}\right]_E}{\left[\frac{1}{\langle A \rangle} + \frac{1}{\langle B \rangle}\right]_{E_{\text{ref}}}}, \quad (18)$$

where E_{ref} is the energy at which the reference value of ν_{dyn} was chosen and E denotes the energy at which the value of ν_{dyn} is estimated. The energy dependence predicted by Eq. (18), with a reference energy of $E_{\text{ref}} = \sqrt{s_{N+N}} \approx 6.3$ GeV (corresponding to 20A GeV laboratory energy), is illustrated for $\nu_{\text{dyn}}[p + \bar{p}, \pi^+ + \pi^-]$ and $\nu_{\text{dyn}}[K^+ + K^-, \pi^+ + \pi^-]$ in Figs. 11(a) and 11(c) by the green curves. However, this

TABLE VI. Numerical values of $\nu_{\text{dyn}}[K^+ + K^-, \pi^+ + \pi^-]$ with statistical and systematic error estimates.

	$\nu_{\text{dyn}} (10^{-3})$	$\sigma_{\text{stat.}} (10^{-3})$	$\sigma_{\text{sys.}} (10^{-3})$
20A GeV	11.738	± 2.207	+3.647 -4.183
30A GeV	5.651	± 0.943	+2.672 -0.972
40A GeV	3.41816	± 0.485	+1.241 -0.569
80A GeV	1.564	± 0.322	+0.225 -0.212
160A GeV	1.523	± 0.257	± 0.139

scaling prescription cannot reproduce the sign change observed for the energy dependence of $\nu_{\text{dyn}}[K^+ + K^-, p + \bar{p}]$ as shown in Fig. 11(b). Moreover, using the multiplicities of Table II and the corresponding numbers for the STAR experiment [26] one would expect only about a factor 2 decrease of the value of $\nu_{\text{dyn}}[K^+ + K^-, \pi^+ + \pi^-]$ at $\sqrt{s_{N+N}} = 7.6$ GeV which does not lead to agreement with the STAR result.

Next, the sensitivity of ν_{dyn} to the covered regions of phase space will be studied since these differ for the NA49 and STAR measurements. As an example Fig. 12 illustrates the phase space coverage for pions, kaons and protons at 30A GeV projectile energy in the acceptance of the NA49 detector. The acceptance coverage for all other energies is provided in Ref. [24] in terms of acceptance matrices. Fig. 12 also presents the acceptance of the STAR apparatus at corresponding center-of-mass energy is presented by colored lines. The dependence of ν_{dyn} on the selected phase space region was studied by performing the analysis in different phase space bins stretching from a forward rapidity cut to mid-rapidity. Technically different phase space bins were selected by applying upper momentum cuts to the reconstructed tracks where the cut value corresponded to the momentum of a proton at $p_{\perp} = 0$ with a chosen maximum rapidity. Thereafter this quantity will be called a proton rapidity cut. The upper panels of Fig. 12 illustrate one such phase space bin for 30A GeV Pb + Pb data. The reconstructed value of $\nu_{\text{dyn}}[K^+ + K^-, p + \bar{p}]$ in this bin is plotted as a red square in Fig. 13. Similarly the green square in Fig. 13 represents the reconstructed value of $\nu_{\text{dyn}}[K^+ + K^-, p + \bar{p}]$ corresponding to the phase space bin plotted in the lower panel of Fig. 12. Note that in this particular bin the NA49 point is consistent with the STAR result, which is shown by the purple star. This study demonstrates a strong dependence of the resulting value of ν_{dyn} on the phase space covered by the measurement. Fig. 14 shows the dependence of ν_{dyn} for different combinations of particles at different energies. At 20A and 30A GeV $\nu_{\text{dyn}}[K^+ + K^-, p + \bar{p}]$ and $\nu_{\text{dyn}}[K^+ + K^-, \pi^+ + \pi^-]$ show a strong dependence on the extent of the phase space region and eventually hit the STAR point in a particular bin. Interestingly the acceptance dependence weakens above 30A GeV where no difference was observed with STAR. It is also remarkable that $\nu_{\text{dyn}}[p + \bar{p}, \pi^+ + \pi^-]$ shows little dependence on the covered phase space region. This detailed study of ν_{dyn} in different phase space regions appears to explain to a large extent the difference between the STAR BES and NA49 measurements.

Differences between NA49 and STAR results are observed when kaons are involved. It is admittedly difficult to separate kaons from protons by dE/dx measurements in the relativistic rise region. In the previous NA49 analysis [11,12] a simplified fitting procedure was applied event-by-event and the deficiencies of the method were approximately corrected by subtracting similarly obtained results from mixed events. In the present analysis a sophisticated fit procedure was used to extract the contributions of different particle species from the inclusive dE/dx distributions. This method was carefully checked and verified with time-of-flight measurements in the limited acceptance region of the TOF detectors. The

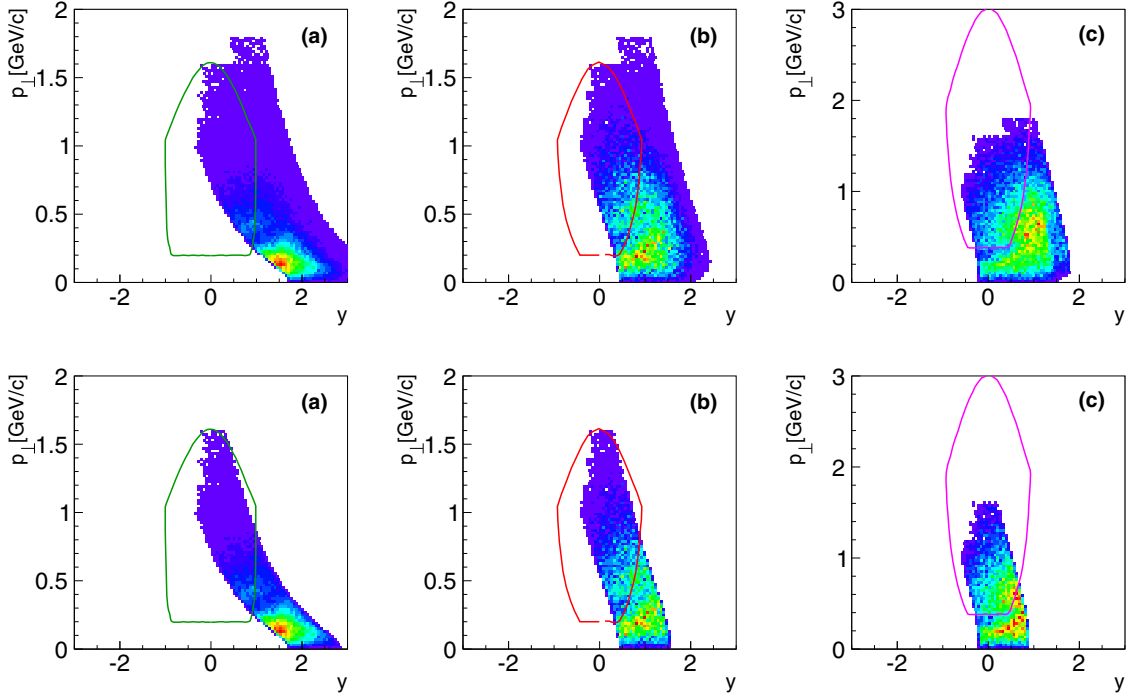


FIG. 12. (Color Online) Phase-space coverage for identified (a) pions, (b) kaons, and (c) protons in the acceptance of the NA49 experiment for Pb + Pb collisions at 30A GeV/c (upper panels). Lower panels illustrate an example of a restriction of the phase-space coverage to better match the region covered by STAR (indicated by solid lines) at the corresponding beam energy.

identity method was applied to determine the moments of the multiplicity distributions and to unfold the effect of the finite resolution of the dE/dx measurements. In spite of the important differences between the two analysis methods the final results are consistent.

Some final remarks are in order concerning the properties and the significance of the fluctuation measure ν_{dyn} . To reveal the physics underlying the studied event-by-event fluctua-

tions, the fluctuation signals measured in heavy-ion (A+A) collisions should be compared systematically to a reference from nucleon-nucleon (N+N) collisions at corresponding energies per nucleon. It is however important to properly take into account trivial differences between A+A and N+N collisions e.g. in the size of the colliding systems. An additional complication in the experimental study of fluctuations in A+A collisions are unavoidable volume fluctuations from event to event. To take account of these considerations a set of “strongly intensive” fluctuation measures has been proposed in Ref. [27]. In fact, the scaled ν_{dyn} (see Eq. (18)) is related to the strongly intensive measure Σ^{AB} (cf. Eq. (13) in Ref. [27])

$$\nu_{\text{dyn}}[A, B]^{\text{Scaled}} \equiv \frac{\nu_{\text{dyn}}[A, B]}{\frac{1}{\langle A \rangle} + \frac{1}{\langle B \rangle}} = \Sigma^{AB} - 1. \quad (19)$$

Future studies of strongly intensive measures may lead to a better understanding of the underlying source of correlations.

IX. SUMMARY

In summary several scenarios were investigated to understand the differences between the NA49 and STAR measurements of the excitation functions of $\nu_{\text{dyn}}[K^+ + K^-, p + \bar{p}]$ and $\nu_{\text{dyn}}[K^+ + K^-, \pi^+ + \pi^-]$. For this purpose the particle identification procedure formerly employed by NA49 was replaced by a different approach, the *identity method*, to reconstruct the fluctuation measure ν_{dyn} . The increasing trend of $\nu_{\text{dyn}}[K^+ + K^-, p + \bar{p}]$ and $\nu_{\text{dyn}}[K^+ + K^-, \pi^+ + \pi^-]$ towards lower energies reported in previous publications of NA49 in terms of the quantity σ_{dyn} was confirmed by this analysis. A detailed study of ν_{dyn} reveals a strong dependence on the

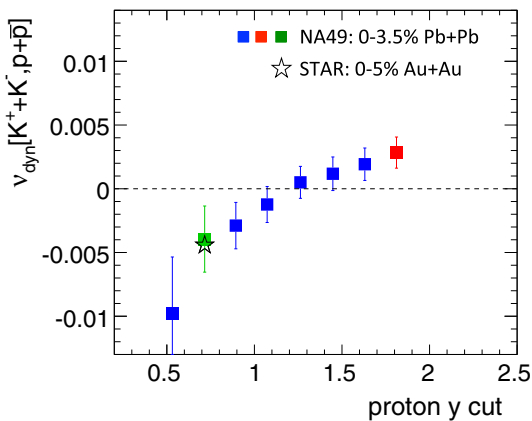


FIG. 13. (Color Online) Phase-space dependence of $\nu_{\text{dyn}}[K^+ + K^-, p + \bar{p}]$ for 30A GeV Pb + Pb collisions of NA49. Red and green squares correspond to the phase-space bins illustrated in the upper and lower panels of Fig. 12 respectively. Blue squares are the NA49 results for other phase-space bins. The result of the STAR experiment is plotted as the purple star at the corresponding NA49 phase-space bin. The phase-space region of the analysis is varied by an upper cut on the momentum (see text).

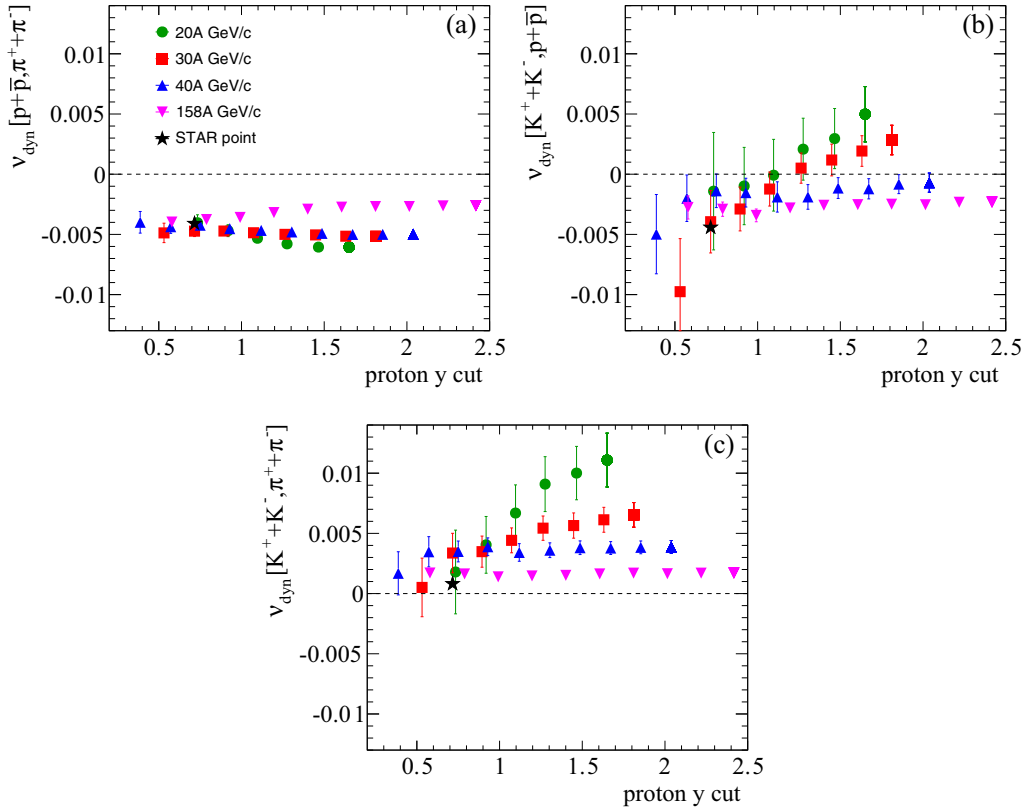


FIG. 14. (Color Online) Phase-space region dependence of (a) $v_{\text{dyn}}[p + \bar{p}, \pi^+ + \pi^-]$, (b) $v_{\text{dyn}}[K^+ + K^-, p + \bar{p}]$, and (c) $v_{\text{dyn}}[K^+ + K^-, \pi^+ + \pi^-]$ in central Pb + Pb collisions of NA49 (triangles, squares, dots). Stars show measurements of the STAR collaboration. Results are plotted versus the maximum proton rapidity (see text).

phase-space coverage at low energies for $v_{\text{dyn}}[K^+ + K^-, p + \bar{p}]$ and $v_{\text{dyn}}[K^+ + K^-, \pi^+ + \pi^-]$ which might explain the different energy dependences measured by NA49 (central Pb + Pb collisions) and STAR (BES program for central Au + Au collisions). As an outlook it is worth mentioning that, since the identity method reconstructs first and second moments of the multiplicity distributions of identified particles, one will be able to investigate the energy dependence of all the fluctuation measures proposed in Ref. [27]. These quantities are better suited for phase transition studies because (within the grand canonical ensemble) they depend neither on the volume nor on its fluctuations which cannot be tightly controlled in experiments.

ACKNOWLEDGMENTS

This work was supported by the US Department of Energy Grant No. DE-FG03-97ER41020/A000, the Bundesministerium für Bildung und Forschung (06F 137), Germany, the German Research Foundation (Grant No. GA 1480/2.1), the National Science Centre, Poland (Grants No. DEC-2011/03/B/ST2/02617 and No. DEC-2011/03/B/ST2/02634), the Hungarian Scientific Research Foundation (Grants No. OTKA 68506, No. 71989, No. A08-77719, and No. A08-77815), the Bolyai Research Grant, the Bulgarian National Science Fund (Ph-09/05), the Croatian Ministry of Science, Education and Sport (Project 098-0982887-2878) and Stichting FOM, the Netherlands.

[1] J. C. Collins and M. J. Perry, *Phys. Rev. Lett.* **34**, 1353 (1975).
 [2] E. V. Shuryak, *Phys. Rep.* **61**, 71 (1980); **115**, 151 (1984).
 [3] For recent results see C. Schmidt (RBC-Bielefeld and HotQCD Collaborations), *Nucl. Phys. A* **820**, 41c (2009); Z. Fodor and S. Katz (Wuppertal Collaboration), *Acta Phys. Pol. B* **42**, 2791 (2011).
 [4] M. Stephanov, *Int. J. Mod. Phys. A* **20**, 4387 (2005).
 [5] M. Stephanov, K. Rajagopal, and E. Shuryak, *Phys. Rev. D* **60**, 114028 (1999).
 [6] V. Koch, [arXiv:0810.2520](https://arxiv.org/abs/0810.2520).
 [7] U. Heinz and M. Jacob, [arXiv:nucl-th/0002042](https://arxiv.org/abs/nucl-th/0002042).

[8] M. Gazdzicki and M. Gorenstein, *Acta Phys. Pol. B* **30**, 2705 (1999).
 [9] C. Alt *et al.* (NA49 Collaboration), *Phys. Rev. C* **77**, 024903 (2008).
 [10] A. Rustamov, *Central Eur. J. Phys.* **10**, 1267 (2012).
 [11] C. Alt *et al.* (NA49 Collaboration), *Phys. Rev. C* **79**, 044910 (2009).
 [12] T. Anticic *et al.* (NA49 Collaboration), *Phys. Rev. C* **83**, 061902(R) (2011).
 [13] T. Anticic *et al.* (NA49 Collaboration), *Phys. Rev. C* **87**, 024902 (2013).

- [14] C. Pruneau, S. Gavin, and S. Voloshin, *Phys. Rev. C* **66**, 044904 (2002).
- [15] T. Tarnowsky (STAR Collaboration), *J. Phys. G: Nucl. Part. Phys.* **38**, 124054 (2011).
- [16] M. Gaździcki, K. Grebieszko, M. Maćkowiak, and S. Mrówczyński, *Phys. Rev. C* **83**, 054907 (2011).
- [17] M. I. Gorenstein, *Phys. Rev. C* **84**, 024902 (2011).
- [18] S. Afanasiev *et al.* (NA49 Collaboration), *Nucl. Instrum. Methods A* **430**, 210 (1999).
- [19] K. J. Eskola, K. Kajantie, and J. Lindfors, *Nucl. Phys. B* **323**, 37 (1989).
- [20] L. Landau, *J. Phys. (USSR)* **8**, 201 (1944).
- [21] T. Anticic *et al.* (NA49 Collaboration), *Phys. Rev. C* **83**, 014901 (2011).
- [22] <https://edms.cern.ch/document/816033>, <https://edms.cern.ch/document/815871>, <https://edms.cern.ch/document/1352820>.
- [23] A. Rustamov and M. I. Gorenstein, *Phys. Rev. C* **86**, 044906 (2012).
- [24] <https://edms.cern.ch/document/1311963/1>.
- [25] V. Koch and T. Schuster, *Phys. Rev. C* **81**, 034910 (2010).
- [26] T. Tarnowsky (private communication).
- [27] M. I. Gorenstein and M. Gaździcki, *Phys. Rev. C* **84**, 014904 (2011).